

Three-dimensional electronic microfliers inspired by wind-dispersed seeds

<https://doi.org/10.1038/s41586-021-03847-y>

Received: 6 January 2021

Accepted: 22 July 2021

Published online: 22 September 2021

 Check for updates

Bong Hoon Kim^{1,2,32}, Kan Li^{3,4,32}, Jin-Tae Kim^{5,32}, Yoonseok Park^{5,32}, Hokyung Jang⁶, Xueju Wang⁷, Zhaoqian Xie^{8,9}, Sang Min Won¹⁰, Hong-Joon Yoon⁵, Geumbee Lee⁵, Woo Jin Jang¹¹, Kun Hyuck Lee⁵, Ted S. Chung⁵, Yeil Hwan Jung¹², Seung Yun Heo⁵, Yechan Lee¹³, Juyun Kim¹¹, Tengfei Cai¹⁴, Yeonha Kim¹¹, Poom Prasopsukh¹⁴, Yongjoon Yu⁵, Xinge Yu¹⁵, Raudel Avila^{16,17,18}, Haiwen Luan^{5,16,17,18}, Honglie Song¹⁹, Feng Zhu²⁰, Ying Zhao²¹, Lin Chen²², Seung Ho Han²³, Jiwoong Kim^{1,2}, Soong Ju Oh²⁴, Heon Lee²⁴, Chi Hwan Lee^{25,26,27}, Yonggang Huang^{16,17,18}, Leonardo P. Chamorro¹⁴, Yihui Zhang¹⁹ & John A. Rogers^{5,17,18,28,29,30,31}

Large, distributed collections of miniaturized, wireless electronic devices^{1,2} may form the basis of future systems for environmental monitoring³, population surveillance⁴, disease management⁵ and other applications that demand coverage over expansive spatial scales. Aerial schemes to distribute the components for such networks are required, and—inspired by wind-dispersed seeds⁶—we examined passive structures designed for controlled, unpowered flight across natural environments or city settings. Techniques in mechanically guided assembly of three-dimensional (3D) mesostructures^{7–9} provide access to miniature, 3D fliers optimized for such purposes, in processes that align with the most sophisticated production techniques for electronic, optoelectronic, microfluidic and microelectromechanical technologies. Here we demonstrate a range of 3D macro-, meso- and microscale fliers produced in this manner, including those that incorporate active electronic and colorimetric payloads. Analytical, computational and experimental studies of the aerodynamics of high-performance structures of this type establish a set of fundamental considerations in bio-inspired design, with a focus on 3D fliers that exhibit controlled rotational kinematics and low terminal velocities. An approach that represents these complex 3D structures as discrete numbers of blades captures the essential physics in simple, analytical scaling forms, validated by computational and experimental results. Battery-free, wireless devices and colorimetric sensors for environmental measurements provide simple examples of a wide spectrum of applications of these unusual concepts.

¹Department of Organic Materials and Fiber Engineering, Soongsil University, Seoul, Republic of Korea. ²Department of Smart Wearable Engineering, Soongsil University, Seoul, Republic of Korea. ³Department of Engineering, University of Cambridge, Cambridge, UK. ⁴State Key Laboratory of Digital Manufacturing Equipment and Technology, Huazhong University of Science and Technology, Wuhan, People's Republic of China. ⁵Querrey Simpson Institute for Bioelectronics, Northwestern University, Evanston, IL, USA. ⁶Department of Electrical and Computer Engineering, University of Wisconsin Madison, Madison, WI, USA. ⁷Department of Materials Science and Engineering, Institute of Materials Science, University of Connecticut, Storrs, CT, USA. ⁸State Key Laboratory of Structural Analysis for Industrial Equipment, Department of Engineering Mechanics, Dalian University of Technology, Dalian, People's Republic of China. ⁹Ningbo Institute of Dalian University of Technology, Ningbo, People's Republic of China. ¹⁰Department of Electrical and Computer Engineering, Sungkyunkwan University, Suwon, Republic of Korea. ¹¹Department of Chemical and Biomolecular Engineering, University of Illinois, Urbana, IL, USA. ¹²Department of Electronic Engineering, Hanyang University, Seoul, Republic of Korea. ¹³Department of Chemical and Biomolecular Engineering, Korea Advanced Institute of Science and Technology, Daejeon, Republic of Korea. ¹⁴Department of Mechanical Science and Engineering, University of Illinois, Urbana, IL, USA. ¹⁵Department of Biomedical Engineering, City University of Hong Kong, Hong Kong, China. ¹⁶Department of Civil and Environmental Engineering, Northwestern University, Evanston, IL, USA. ¹⁷Department of Mechanical Engineering, Northwestern University, Evanston, IL, USA. ¹⁸Department of Materials Science and Engineering, Northwestern University, Evanston, IL, USA. ¹⁹Applied Mechanics Laboratory, Department of Engineering Mechanics, Center for Flexible Electronics Technology, Tsinghua University, Beijing, People's Republic of China. ²⁰School of Logistics Engineering, Wuhan University of Technology, Wuhan, People's Republic of China. ²¹School of Aerospace Engineering and Applied Mechanics, Tongji University, Shanghai, People's Republic of China. ²²State Key Laboratory for Mechanical Behavior of Materials, School of Material Science and Engineering, Xi'an Jiaotong University, Xi'an, People's Republic of China. ²³Electronic Convergence Materials and Device Research Center, Korea Electronics Technology Institute, Seongnam, Republic of Korea. ²⁴Department of Materials Science and Engineering, Korea University, Seoul, Republic of Korea. ²⁵Weldon School of Biomedical Engineering, Purdue University, West Lafayette, IN, USA. ²⁶School of Mechanical Engineering, Purdue University, West Lafayette, IN, USA. ²⁷School of Materials Engineering, Purdue University, West Lafayette, IN, USA. ²⁸Department of Biomedical Engineering, Northwestern University, Evanston, IL, USA. ²⁹Department of Neurological Surgery, Northwestern University, Evanston, IL, USA. ³⁰Department of Chemistry, Northwestern University, Evanston, IL, USA. ³¹Department of Electrical Engineering and Computer Science, Northwestern University, Evanston, IL, USA. ³²These authors contributed equally: Bong Hoon Kim, Kan Li, Jin-Tae Kim, Yoonseok Park. ✉e-mail: y-huang@northwestern.edu; lpchamo@illinois.edu; yihui.zhang@tsinghua.edu.cn; jrogers@northwestern.edu

Plants spread their seeds through a remarkable variety of passive strategies, each the result of sustained processes of natural selection. Botanists classify these methods according to their vectors for dispersal, the main types of which are gravity, mechanical propulsion, wind, water and animals. Among these, wind is one of the most powerful and widely applicable. The 3D shapes of seeds optimized to exploit air flow in such contexts can support stable dynamics in controlled free fall and/or facilitate transport over distances of up to hundreds of kilometres^{10–12}. Although certain interactions between dandelion seeds and the ambient air are known¹³, the flow physics of mediated flight of other classes of wind-dispersed seeds, such as those of *Tristellateia* (woody vines), are not well understood, nor have they been explored for dispersal of microsystems technologies^{14,15}. Just as plants use seeds and passive mechanisms for dispersal of genetic material to propagate the species, interesting opportunities might follow from use of similar approaches to distribute miniature electronic sensors, wireless communication nodes, energy harvesting components and/or various internet-of-things (IoT) technologies as monitors to track environmental processes, as aids to guide remediation efforts or as components to support distributed surveillance. This paper introduces foundational engineering science for practical realization of these ideas^{16–20}.

Wind-dispersed seeds adopt geometries that can be interpreted as evolutionary solutions to a physical problem governed by gravity and an immobile lifeform, optimizing dynamic stability and/or transport distance during passive free fall²¹. The character of motions induced by air flow defines four broad categories of seeds: (i) gliders such as those of the Javan cucumber (*Alsomitra macrocarpa*), (ii) helicopters such as those of the box elder (*Acer negundo*) and the big-leaf maple (*Acer macrophyllum*), the tristellateia (*Tristellateia australasiae*) (iii) parachuters such as those of the dandelion (*Taraxacum officinale*) and the western salsify (*Tragopogon dubius*), and (iv) flutterers/spinners such as those of the empress tree (*Paulownia tomentosa*), the tree of heaven (*Ailanthus altissima*) and the jacaranda (*Jacaranda mimosifolia*) (Fig. 1a,b). These designs serve as inspiration for human-made passive flier structures engineered to optimize aerial dispersal of functional payloads. The overall sizes span the microscale (with half-widths of wings <1 mm; microfliers), mesoscale (half-widths of about 1 mm; mesofliers), and macroscale (half-widths >1 mm; macrofliers) with the capacity to integrate material elements and devices with critical feature sizes that extend into the nanometre regime. Figure 1b compares the dimensions and the geometries of a representative 3D microflier to those of various seeds with elaborate designs.

The fabrication scheme exploits processes of controlled mechanical buckling to convert planar precursor structures formed with state-of-the-art planar processing and lithographic techniques into desired 3D layouts. Specifically, releasing the strain in a prestretched elastomer substrate generates compressive forces on these precursors through a collection of bonding sites. The result causes geometrical transformation through a continuous sequence of in- and out-of-plane displacements and rotational motions (Fig. 1c–e). When implemented with shape memory polymers (SMPs; a mixture of epoxy monomer (E44, Methods), curing agent (D230, Methods)) and sacrificial thin layers (Mg, about 50 nm) at the bonding sites, the resulting 3D objects can be released as free-standing passive fliers (Fig. 1f)²⁰. The designs and choices of bonding sites define the overall 3D architectures; the magnitude of strain release determines the extent of three dimensionality, qualitatively defined by the ratio of the height of the structures to their lateral dimensions (small, ‘3D’; large, ‘3D+’), as in Fig. 1c. This scheme provides access to systems that behave in any of the three bio-inspired modalities mentioned previously, with flat and/or curved wings, solid and/or perforated structural elements, and various numbers of articulations. A simple identifying nomenclature includes (i) a number to indicate the number of wings, (ii) a letter to describe the shape of wings (R = ribbons, M = membranes, PM = porous membranes

and H = hybrid, a combination of ribbons and membranes), and (iii) a number to define the 3D aspect ratio (for example, height divided by width). Figure 1d shows pictures of three 3D microfliers (widths of about 500 μm) placed on a fingertip. Figure 1e highlights a 10 × 10 array of micro- and mesofliers of various sizes (widths of about 0.5–2 mm; Extended Data Fig. 1) and geometries, formed via a single assembly process. Mass quantities of fliers can be formed at high throughput (Fig. 1f). 3D porous mesofliers with terminal velocities (v_T) that are much smaller than other objects with similar sizes and types are possible (Fig. 1g, Supplementary Video 1)²².

Computational fluid dynamics (CFD) simulations (Methods, Extended Data Fig. 2, Supplementary Fig. 2) and analytical approaches (Fig. 2a, Supplementary Note 1) capture the underlying aerodynamic mechanisms. The drag coefficient, $C_D = W / (0.5\rho v_T^2 A)$, is a dimensionless parameter that characterizes the relationship between the terminal velocity (v_T) and the weight (W), where ρ is the density of air and A is the area of the 2D membrane of the flier, excluding the area of perforations (that is, voids). Figure 2b summarizes values of C_D computed by CFD at different Reynolds numbers ($Re = 2r\rho v_T / \mu$, where μ is the dynamic viscosity of air and $2r$ is the diameter of the flier). The empirical relationship $C_D \approx G_0 + G_1/Re$ applies below the transition region ($Re \approx 10^5$)²³. The first (G_0) and second (G_1/Re) terms correspond to the inertial and viscous effects, at high and low Re , respectively. v_T can be expressed as

$$v_T \approx -\frac{\mu G_1}{4r\rho G_0} + \sqrt{\left(\frac{\mu G_1}{4r\rho G_0}\right)^2 + \frac{2W}{\rho A G_0}} \quad (1)$$

where G_0 and G_1 depend on geometric parameters of the fliers (Extended Data Fig. 3), such as the areal fill factor ($\eta = A_0/\pi r^2$, where A_0 is the void-free membrane area), porosity ($p = A_{\text{void}}/A_0$, where A_{void} is the total area of voids) and the tilt angle of the blades (β) in the rotational direction. In particular, for macrofliers, equation (1) becomes

$$v_T \approx \sqrt{\frac{2W}{\rho A G_0}} \quad (2)$$

while for meso- and microfliers,

$$v_T \approx \frac{4rW}{\mu A G_1} \quad (3)$$

consistent with CFD simulations (Supplementary Figs. 3, 4). CFD results (Fig. 2c) show that flow fields of microfliers ($2r \approx 0.4$ mm, $Re \approx 3$; near the Stokes regime) and mesofliers ($2r \approx 2$ mm, $Re \approx 40$) are laminar; those of macrofliers are turbulent ($2r \approx 40$ mm, $Re \approx 3,000$). Mesofliers with different 3D configurations have a similar dependence of v_T on η (Fig. 2d, Supplementary Fig. 5), due to thick boundary layers at low Re . Porous features, designed to capture effects of parachute-type seeds which incorporate bundles of filaments (for example, dandelion pappus, $p \approx 0.9$), can be introduced through the addition of perforating holes (that is, voids) in the structural components of the fliers. The result enhances C_D and reduces v_T , with different effects on G_0 and G_1 (Fig. 2b, Supplementary Figs. 6, 7, Extended Data Fig. 4 and Supplementary Note 2)¹³. For example, porosity (for example, $p = 0.25$) has a smaller effect on v_T (by about 10%) for macrofliers than for microfliers (by about 20%, Supplementary Fig. 8). By contrast, the effects of curvature and tilt angle (β) in the blades of macrofliers (Supplementary Figs. 9, 10) are more notable than those of microfliers (Supplementary Note 3).

Environmental factors, that is, altitude, humidity, temperature or molecular structure of the air, influence the behaviours mainly through ρ and μ (Supplementary Figs. 11–13). For example, increasing the altitude from 0 to 80 km decreases ρ by a factor of 5 and decreases the value of μ by about 25%. Consequently, mesofliers exhibit small v_T even

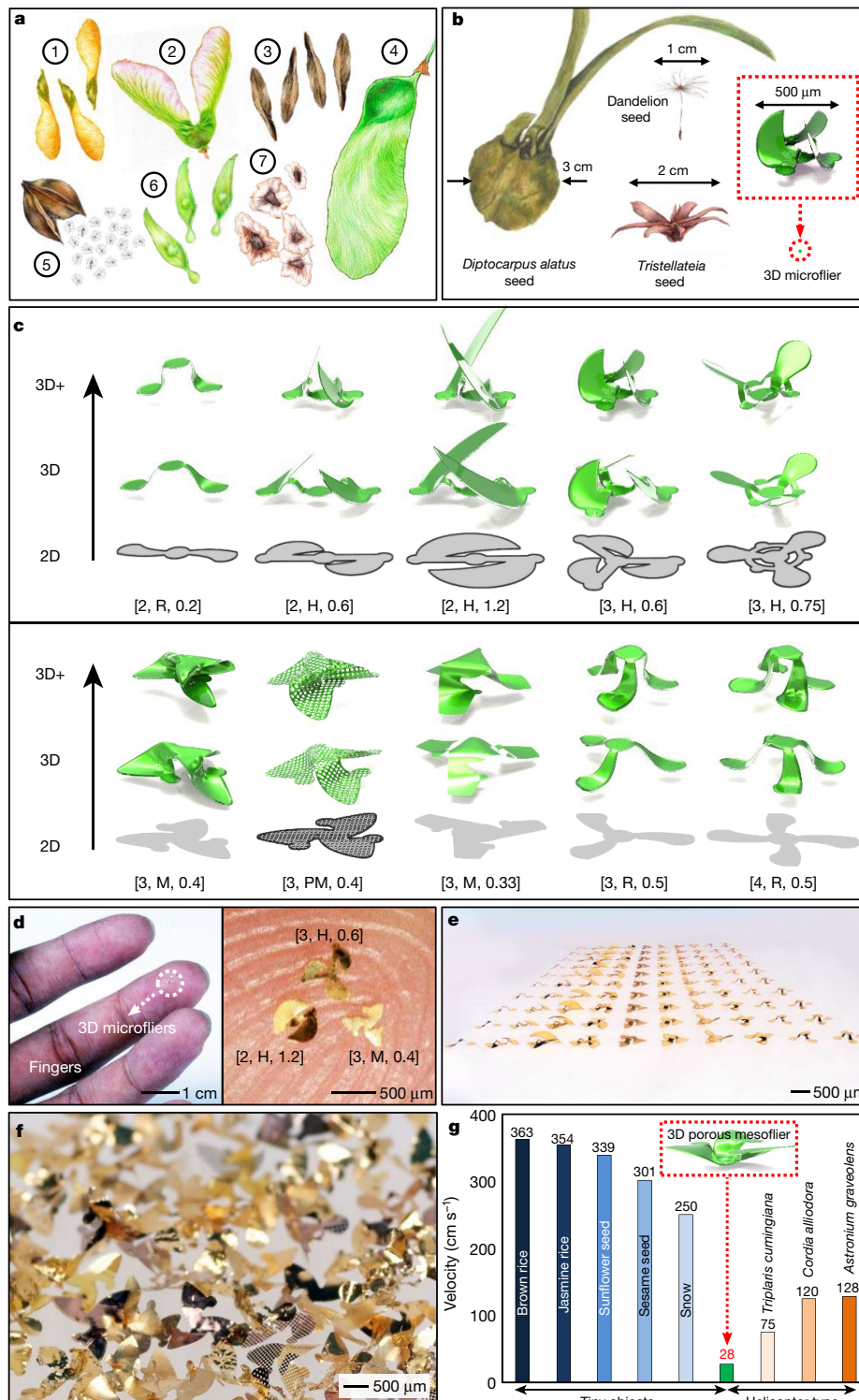


Fig. 1 | 3D microfliers inspired by wind-dispersed seeds. **a**, Helicopter types: (1) the box elder (*Acer negundo*), (2) the big-leaf maple (*Acer macrophyllum*), (3) the evergreen ash (*Fraxinus uhdei*) and (4) the tipu tree (*Tipuana tipu*); flutterers/spinner types: (5) the empress tree (*Paulownia tomentosa*), (6) the tree of heaven (*Ailanthus altissima*) and (7) the jacaranda (*Jacaranda mimosifolia*). **b**, Schematic illustration that compares the sizes and morphologies of helicopter types, a *Diptocarpus alatus* seed and *Tristellateia* seed, a parachute type, dandelion seed, and a representative 3D microfliar (typical size shown in the box). **c**, Mechanical simulation results for the geometrical transformation of ten different 2D precursors (grey; 2D, bottom row) into corresponding 3D structures with modest (green; 3D, middle row) and large (green; 3D+, top row) aspect ratios. The identifying terminology

beneath each case indicates: (i) a number to indicate the number of wings, (ii) a letter to describe the shape of the wings (R, ribbons, M, membranes, PM, porous membranes, and H, hybrid), and (iii) a number to define the 3D aspect ratio (for example, height divided by width). Masses of micro- and mesofliers are listed in Supplementary Table 1. **d**, Photograph and optical micrograph of three different 3D microfliers, [2, H, 1.2], [3, H, 0.6] and [3, M, 0.4]; left, resting on the tip of a finger; and right, shown at higher magnification. **e**, A 10 × 10 array of microfliers. **f**, A large collection of 3D microfliers. **g**, The terminal velocity of several tiny objects (diameters ≈ 1 mm; blue bars), helicopter-type wind-dispersed seeds⁶ (brown bars), and a 3D porous mesofliar [3, PM, 0.4] (green bar) inspired by *Tristellateia* seeds (diameter, about 19.8 mm, mass, 18.2 mg, and density, about 0.11 mg mm⁻³; Supplementary Fig. 1).

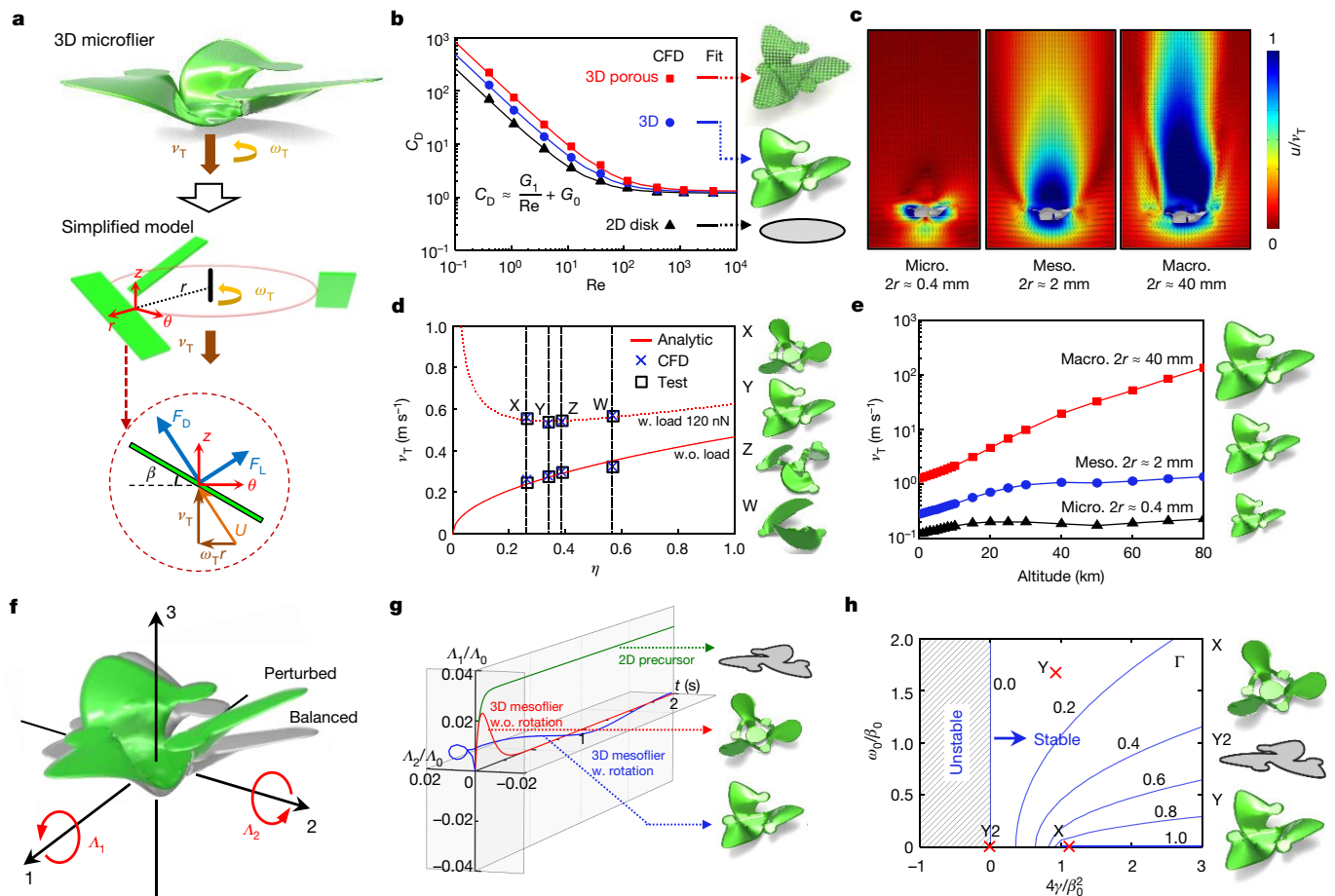


Fig. 2 | Theoretical analysis and numerical simulation of the aerodynamics associated with representative 3D micro-, meso- and macrofliers.

a, Schematic diagram of a rotating 3D flier [3, M, 0.4] (top) and a simplified model (bottom) for purposes of theoretical analysis, decomposing complex flier configurations into discrete tilted blades, with key variables (see definitions in main text and Supplementary Note 1) indicated. The inset shows the cross section of a blade. **b**, Drag coefficient versus Reynolds number of various structures (that is, 2D disk, and 3D microfliers [3, M, 0.4] and [3, PM, 0.4]), with CFD results fitted by empirical equation $C_D \approx \frac{G_1}{Re} + G_0$. **c**, Instantaneous flow fields for 3D micro-, meso- and macrofliers. **d**, Terminal velocities of four different 3D mesofliers, X = [3, H, 0.75], Y = [3, M, 0.4], Z = [3, H, 0.6] and W = [2, H, 1.2] with various fill factors, and with a microscale inorganic LED (-120 nN) as an optional payload (w., with; w.o., without). **e**, CFD prediction of the terminal velocity for 3D fliers [3, M, 0.4] at different size scales at different altitudes in the atmosphere, from sea level to 80 km. **f**, Schematic

diagram of the stability analysis of a rotating 3D flier, [3, M, 0.4], during free fall. Stability can be analysed by considering the flier as a rotating rigid body driven by forces associated with air flow and subjected to small perturbations ($\dot{A}_1 = A_0 \cdot 1s^{-1}$, where $A_{1,2}$ denotes the perturbation angles in directions 1 and 2, and A_0 denotes the amplitude) from an initial balanced state (Supplementary Note 4). **g**, Behaviours of different 3D mesofliers (a 2D precursor for a 3D mesoflier [3, M, 0.4], and 3D mesofliers [3, H, 0.75] (without rotation) and [3, M, 0.4] (with rotation)) with small perturbations of angular speed. **h**, Stability phase plot of 3D mesofliers X = [3, H, 0.75] and Y = [3, M, 0.4] and a 2D precursor for a 3D mesoflier Y2 = [3, M, 0.4]. $\Gamma \equiv \min \left[\text{Real} \left(\left(1 \pm \frac{\omega_0}{\beta_0} i \right) \pm \sqrt{\left(1 \pm \frac{\omega_0}{\beta_0} i \right)^2 - \frac{4\gamma}{\beta_0^2}} \right) \right]$, where $\beta_0 = \frac{\pi \mu r^2}{8 \sqrt{\rho}} \cdot \text{Re} \left(2G_0 + \frac{G_1}{Re} \right) \frac{1}{I_1}$, $\omega_0 = \frac{I_3 - I_2}{I_1} \omega_T$, $\gamma = \frac{wd}{I_1}$. $I_{1,2,3}$ are the moments of inertia for directions 1, 2 and 3, and d is the distance between the centre of gravity and the centre of pressure.

at high altitudes (for example, approximately 1.36 m s^{-1} at 80 km for $2r \approx 2 \text{ mm}$, Fig. 2e), far smaller than those of macrofliers at such altitudes (for example, $>100 \text{ m s}^{-1}$ for $2r \approx 40 \text{ mm}$). Rotational behaviours (for example, rotational speed ω_T) that follow from the 3D configuration (characterized by β , rotation does not occur with $\beta = 0$) affect v_T by reducing G_1 and increasing G_0 (Extended Data Fig. 5), and by conferring kinematic stability. Analytical modelling (Fig. 2f, Supplementary Note 4), validated by CFD (Supplementary Fig. 14), shows that $\omega_T \propto v_T/r$. Studies of three representative structures (that is, a 2D precursor, a 3D mesoflier without rotation and a 3D mesoflier with rotation, all with the same size ($2r \approx 2 \text{ mm}$) and fill factor ($\eta \approx 0.35$) reveal the essential effects. Figure 2g shows the perturbed angles ($A_{1,2}/A_0$) as a function of time (t) after perturbation. The 2D precursor does not return to the balanced state quickly, but the maximum perturbed angle (about 0.025)

is larger than that with rotation (approximately 0.018). A factor $\Gamma = \Gamma \left(\frac{\omega_0}{\beta_0}, \frac{4\gamma}{\beta_0^2} \right)$ can be defined to characterize the stability, in which ω_0 ($\propto \omega_T$), γ and β_0 account respectively for the influence of geometry, material and air properties (Fig. 2h, Supplementary Note 4). A large positive value of Γ corresponds to a structure that can quickly recover to its balanced, stable state; a negative value of Γ corresponds to an unstable structure. The maximum perturbed angle decreases monotonically with ω_0/β_0 (Supplementary Fig. 15), owing to rotational improvements in stability.

Experimental studies reveal detailed features of these and related behaviours. One set of measurements involves 3D particle tracking velocimetry (3D-PTV), with a focus on (i) quantifying the characteristics of aerodynamic stability, and (ii) capturing 3D patterns of flow induced in a quiescent environment (Methods, Extended Data Fig. 6a).

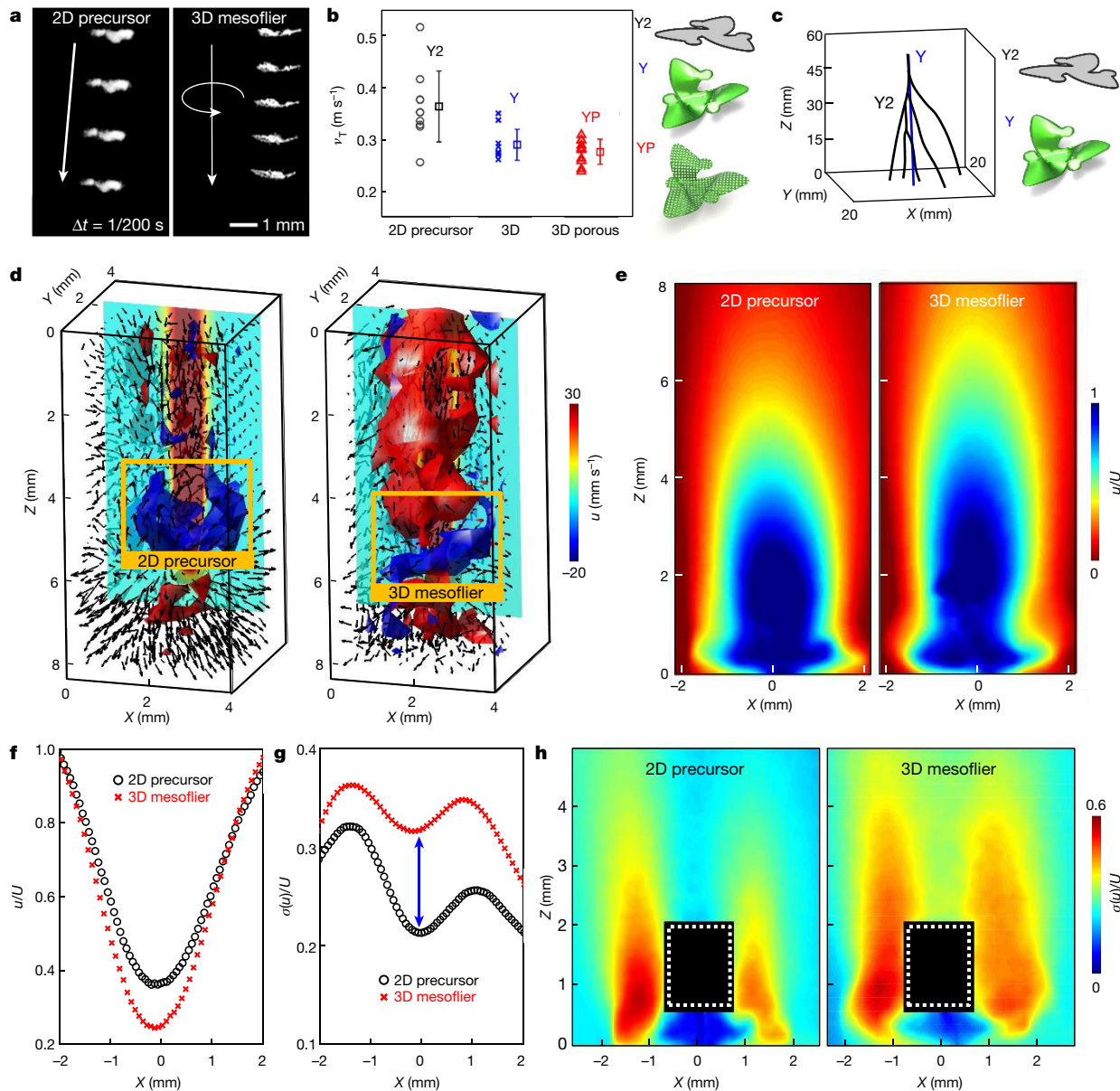


Fig. 3 | Experimental measurements of the flow characteristics of representative 3D mesofliers. **a**, Optical images of Y2 (a 2D precursor for 3D mesoflier [3, M, 0.4]) and the corresponding 3D mesoflier Y ([3, M, 0.4]) at various times during free fall. The former shows non-rotating and random tumbling behaviours; the latter exhibits strong rotational dynamics and a straight path trajectory. **b**, Mean terminal velocity (open squares) and standard deviation (error bars) for Y2 and Y (see **a**), and for YP (a porous 3D mesoflier, [3, PM, 0.4]). The total number of trials for each case is $N=10$. **c**, Falling trajectories of Y2 and Y (see **a**) on release at an angle of 90° , where 0° corresponds to the flat side parallel to the ground. **d**, Instantaneous 3D flow

velocity fields induced by a free-falling Y2 (left) and Y (right) determined via 3D-PTV. Red and blue iso-surfaces indicate iso-values of 15 mm s^{-1} and -5 mm s^{-1} , respectively. The colour denotes correlated CFD results of the in-plane 2D vertical velocity along the centre plane of the flier. PIV measurements of instantaneous flow fields induced by Y2 and Y in a wind tunnel. **e**, Mean velocity fields of a 2D precursor for a 3D mesoflier [3, M, 0.4] (left) and a 3D mesoflier [3, M, 0.4] (right) in these conditions, with a wind velocity $U \approx 0.4 \text{ m s}^{-1}$. **f, g**, Velocity profiles (**f**) and vertical velocity fluctuation profiles (**g**) at $x=4 \text{ mm}$ downstream. **h**, Vertical velocity fluctuation $\sigma(u)$ for a 2D precursor for a 3D mesoflier [3, M, 0.4] (left) and a 3D mesoflier [3, M, 0.4] (right).

Another set focuses on quantifying the wake produced by various fliers placed at the exit of a vertical wind tunnel by high-speed particle image velocimetry (PIV; Methods, Extended Data Fig. 6b, Supplementary Figs. 16, 17, Supplementary Videos 2, 3). Data show that a 2D precursor for a 3D mesoflier [3, M, 0.4], Y2, (diameter $2r=2 \text{ mm}$, weight $W=119 \text{ nN}$) exhibits non-rotating, random tumbling behaviours with v_T ($v_{T,2D} \approx 0.37 \text{ m s}^{-1}$) larger than that of stable, rotational behaviours of a 3D mesoflier [3, M, 0.4], Y (Fig. 3a, Supplementary Videos 4, 5), v_T ($v_{T,3D} \approx 0.29 \text{ m s}^{-1}$). The addition of porosity into the same structure, YP, promotes further reductions in v_T ($v_{T,3Dporous} \approx 0.28 \text{ m s}^{-1}$; $\eta = 0.26$; Fig. 3b), consistent with simulations (Fig. 2c). The 3D

shapes reduce the standard deviation of v_T by about 40% owing to enhanced aerodynamic stability ($\sigma_{2D} \approx 0.06 \text{ m s}^{-1}$, $\sigma_{3D} \approx 0.03 \text{ m s}^{-1}$, $\sigma_{3Dporous} \approx 0.02 \text{ m s}^{-1}$; Fig. 3c). The 3D mesofliers travel in a straight downward direction, while the 2D precursors exhibit chaotic falling behaviours^{24–26}. These latter processes lead to large variations in v_T and in settling location. The 3D wake measured with 3D-PTV further highlights the effects of the rotating 3D mesofliers (Fig. 3d and Supplementary Video 6), correlated with CFD results (Supplementary Fig. 18). Complementary PIV measurements illustrate instantaneous velocity fields (Supplementary Fig. 19), mean velocity distributions (Fig. 3e), velocity profiles (Fig. 3f) and RMS velocity fluctuation profiles

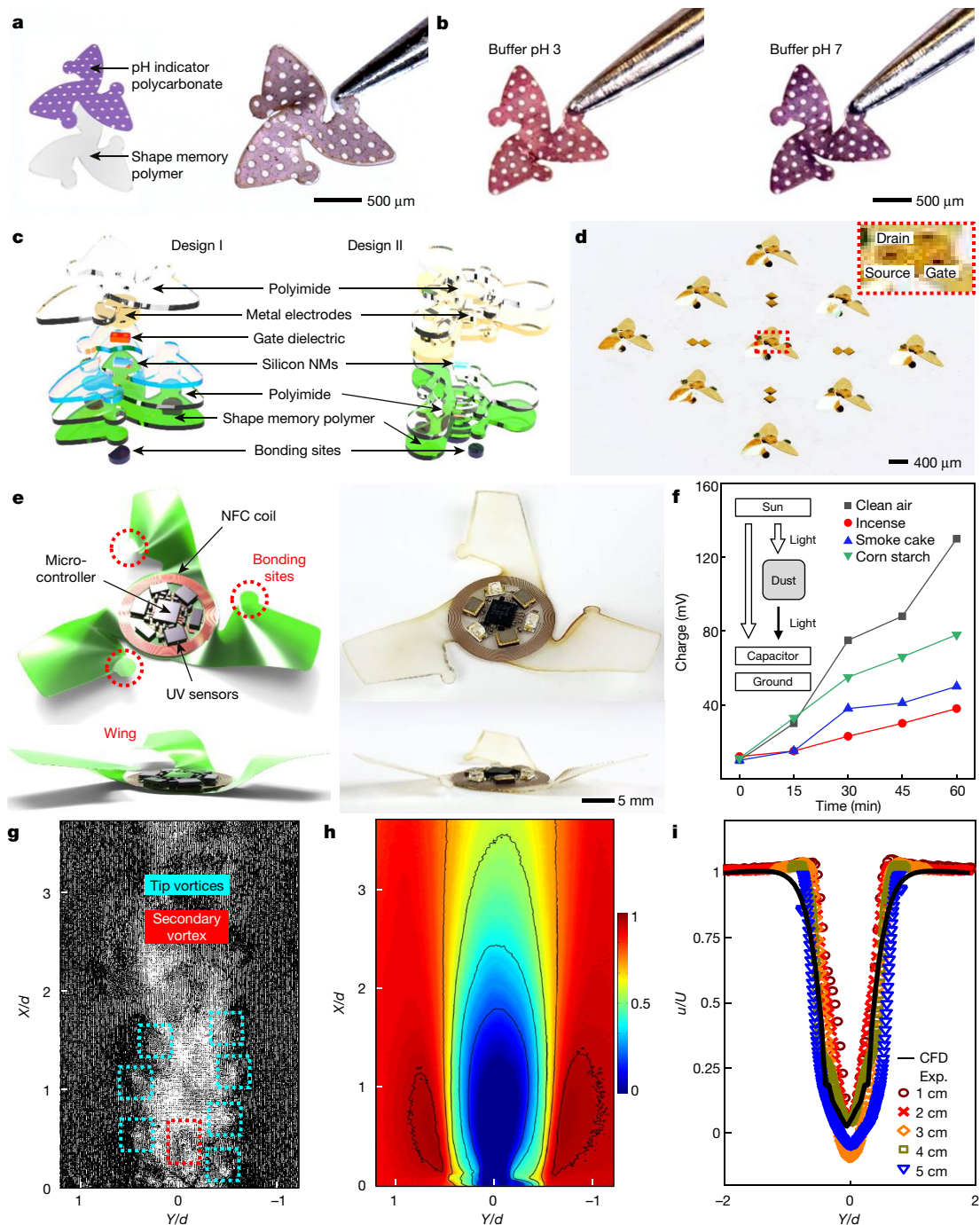


Fig. 4 | 3D colorimetric mesofliers, electronic mesofliers and IoT macrofliers. **a**, Exploded schematic illustration and images of a colorimetric microflier that responds to local pH. **b**, Colour responses of the device at two different pH values. **c**, Optical micrographs of 3D electronic mesofliers [3, M, 0.4] and [3, H, 0.75] with silicon nanomembrane (NM) nMOS transistors and diodes as payloads. **d**, Photograph of a 3 × 3 array of 3D electronic mesofliers [3, M, 0.4] with Si NM nMOSFET payloads (inset). **e**, Mechanical simulation results and photograph of a 3D IoT macroflier with a circuit to

measure fine dust pollution through the light dosimetry method. The weight of the IoT flier is 19.7 mg ($d \approx 5$ cm), with payload 198 mg (Supplementary Fig. 23). **f**, Energy stored in the supercapacitor as a function of exposure time in the presence of three types of fine dust (Methods, Extended Data Fig. 9). **g–i**, High-speed PIV flow measurements for 3D IoT macrofliers ($d = 2$ cm) with various diameters and air velocities; instantaneous velocity field (**g**) and mean velocity field u/U (**h**). **i**, Normalized spanwise velocity profiles at 1.2 diameters downstream for 3D IoT macrofliers with diameters between 1 cm and 5 cm.

(Fig. 3g, h). The 3D mesoflier (Fig. 3e, f) induces a comparatively larger wake and a higher level of vertical velocity fluctuations, $\sigma(u)$, compared to the 2D precursor (Fig. 3g). The fluctuations in the 2D case exhibit an asymmetrical distribution due to its non-rotating behaviour (Fig. 3h), as a distinct source of instability. Symmetry in velocity fluctuations and large momentum deficits are consistent with the advantageous aerodynamics of the 3D mesofliers.

Like seeds, these 3D platforms can transport payloads with passive or active functionality. The fabrication scheme affords many possibilities in functional integration, spanning nearly all forms of planar microsystems, semiconductor technologies and wireless components (Supplementary Table 2). As a simple example capable of remote readout without electronics, Fig. 4a and b shows pH-responsive 3D mesofliers [3, M, 0.4] that use a colour indicator based on anthocyanin infiltrated

into a polycarbonate (PC) membrane (Extended Data Fig. 7)²⁷. Electronics can be easily integrated, as in Fig. 4c, which shows an exploded view illustration of 3D mesofliers, that is, [3, M, 0.4] and [3, H, 0.75], that support semiconductor devices based on silicon nanomembranes (Si NMs; thickness 200 nm) as the active material. These devices comprise: (i) n-channel Si NM metal–oxide semiconductor field effect transistors (nMOSFETs; channel lengths/widths of 20/80 μm) with SiO₂ gate dielectrics (thickness of about 50 nm) and metal electrodes for gate, source and drain (Cr/Au, thickness approximately 5/50 nm); and (ii) Si NM diodes formed from materials similar to those of the nMOSFETs, and which are similar to the devices featured in the CFD simulations (Supplementary Figs. 20–25). The electrical properties are consistent with those expected for monocrystalline silicon devices formed in the usual way on planar wafer substrates (Extended Data Fig. 8). Figure 4d shows pictures of a 3 × 3 array of 3D mesofliers [3, M, 0.4] with Si NM nMOSFETs.

These types of electronic and colorimetric 3D meso- and macrofliers can be released into the atmosphere from positions at high altitudes, in dispersed configurations, for various applications including atmospheric monitoring as a complement to conventional gravimetric and optical particle counting methods^{28,29} performed at localized positions. An example of fliers for such purposes supports wireless, miniaturized battery-free light dosimeters designed for operation in the ultraviolet-A band of the solar spectrum, according to recently reported schemes³⁰. A photodiode generates photocurrent with a magnitude proportional to the ultraviolet-A intensity. This current continuously charges a supercapacitor as a continuous, accumulation mode of detection during and after free fall. The electronics include a system-on-a-chip with near field communication (NFC) capabilities and an analogue-to-digital converter with a general-purpose input/output. An external reader device activates the system-on-a-chip to measure the voltage across the supercapacitor, retrieve the corresponding digital data and to discharge the supercapacitor, all in a single operation (Fig. 4e, Supplementary Figs. 26, 27, Supplementary Table 3). The measured dose depends on atmospheric conditions, including the pollution levels across altitudes, solar activity and other factors. Figure 4f demonstrates the quantitative effect of airborne particles (Extended Data Fig. 9). General strategies for data collection from distributed collections of devices involve radio-frequency wireless links to external reader hardware, such as near-field (Fig. 4e) and far-field schemes that serve as ultralow-power technologies for IoT applications. With colorimetric chemical reagents, readout can occur remotely thorough colour analysis of high-resolution aerial digital images. The aerodynamics of these 3D IoT macrofliers (Fig. 4g–i, Supplementary Figs. 28–31) are consistent with preceding discussions of the physics.

The bio-inspired ideas and engineering foundations for mesoscale 3D fliers introduced here establish a set of unusual capabilities in aerial dispersal of advanced device technologies. The key findings are that: (i) complex bio-inspired 3D structures can be designed and manufactured in geometries that create large momentum deficits in wakes induced by free fall, thereby promoting high drag forces and low terminal velocities; (ii) certain 3D designs induce rotational motions that eliminate instabilities associated with chaotic falling behaviours such as fluttering and tumbling; (iii) the physics associated with (i) and (ii) applies to 3D structures with dimensions in the millimetre range, even for cases near or within the Stokes regime; and (iv) analysis approaches that simplify complex 3D configurations into discrete tilted blades can capture the essential physics, including the aerodynamic dependence on the geometric and environmental parameters at different Re. Although not explicitly studied in this research, the effects of wind represent important practical considerations that tend to increase in significance as the sizes and the masses of the fliers decrease. Gliders and parachuters represent alternative platforms that can be realized using similar approaches. Layouts that

combine these various design strategies may offer enhanced levels of performance, beyond those observed in nature. For many applications of distributed sensors and electronic components, efficient methods for recovery and disposal must be carefully considered. One solution that bypasses these issues exploits devices constructed from materials that naturally resorb into the environment via a chemical reaction and/or physical disintegration to benign end products^{31,32}. In these and other cases, ecosystem-resorbable piezoelectric actuators or alternative active mechanical components may enhance control over flight dynamics. Such possibilities represent promising directions for future work.

Online content

Any methods, additional references, Nature Research reporting summaries, source data, extended data, supplementary information, acknowledgements, peer review information; details of author contributions and competing interests; and statements of data and code availability are available at <https://doi.org/10.1038/s41586-021-03847-y>.

1. Chung, H. U. et al. Binodal, wireless epidermal electronic systems with in-sensor analytics for neonatal intensive care. *Science* **363**, eaau0780 (2019).
2. Kim, B. H. et al. Mechanically guided post-assembly of 3D electronic systems. *Adv. Funct. Mater.* **28**, 1803149 (2018).
3. Jin, J., Wang, Y., Jiang, H. & Chen, X. Evaluation of microclimatic detection by a wireless sensor network in forest ecosystems. *Sci. Rep.* **8**, 16433 (2018).
4. González-Alcaide, G., Llorente, P. & Ramos-Rincón, J. M. Systematic analysis of the scientific literature on population surveillance. *Heliyon* **6**, E05141 (2020).
5. Groseclose, S. L. & Buckeridge, D. L. Public health surveillance systems: recent advances in their use and evaluation. *Annu. Rev. Public Health* **38**, 57–79 (2017).
6. Augspurger, C. K. Morphology and dispersal potential of wind-dispersed diaspores of neotropical trees. *Am. J. Bot.* **73**, 353–363 (1986).
7. Won, S. M. et al. Multimodal sensing with a three-dimensional piezoresistive structure. *ACS Nano* **13**, 10972–10979 (2019).
8. Kim, B. H. et al. Three-dimensional silicon electronic systems fabricated by compressive buckling process. *ACS Nano* **12**, 4164–4171 (2018).
9. Park, Y. et al. Three-dimensional, multifunctional neural interfaces for cortical spheroids and engineered assembloids. *Sci. Adv.* **7**, eabf9153 (2021).
10. Nathan, R. et al. Mechanisms of long-distance dispersal of seeds by wind. *Nature* **418**, 409–413 (2002).
11. Nathan, R. Long-distance dispersal of plants. *Science* **313**, 786–788 (2006).
12. Seale, M. & Nakayama, N. From passive to informed: mechanical mechanisms of seed dispersal. *New Phytol.* **225**, 653–658 (2020).
13. Cummins, C. et al. A separated vortex ring underlies the flight of the dandelion. *Nature* **562**, 414–418 (2018).
14. Rabault, J., Fauli, R. A. & Carlson, A. Curving to fly: synthetic adaptation unveils optimal flight performance of whirling fruits. *Phys. Rev. Lett.* **122**, 024501 (2019).
15. Fauli, R. A., Rabault, J. & Carlson, A. Effect of wing fold angles on the terminal descent velocity of double-winged autorotating seeds, fruits, and other diaspores. *Phys. Rev. E* **100**, 013108 (2019).
16. Xu, S. et al. Assembly of micro/nanomaterials into complex, three-dimensional architectures by compressive buckling. *Science* **347**, 154–159 (2015).
17. Zhang, Y. et al. A mechanically driven form of kirigami as a route to 3D mesostructures in micro/nanomembranes. *Proc. Natl Acad. Sci. USA* **112**, 11757–11764 (2015).
18. Zhang, Y. et al. Printing, folding and assembly methods for forming 3D mesostructures in advanced materials. *Nat. Rev. Mater.* **2**, 17019 (2017).
19. Pang, W. et al. Electro-mechanically controlled assembly of reconfigurable 3D mesostructures and electronic devices based on dielectric elastomer platforms. *Natl Sci. Rev.* **7**, 342–354 (2020).
20. Wang, X. et al. Freestanding 3D mesostructures, functional devices, and shape-programmable systems based on mechanically induced assembly with shape memory polymers. *Adv. Mater.* **31**, 1805615 (2019).
21. Greene, D. F. & Johnson, E. A. Seed mass and dispersal capacity in wind-dispersed diaspores. *Oikos* **67**, 69–74 (1993).
22. Zhang, L., Wang, X., Moran, M. D. & Feng, J. Review and uncertainty assessment of size-resolved scavenging coefficient formulations for below-cloud snow scavenging of atmospheric aerosols. *Atmos. Chem. Phys.* **13**, 10005–10025 (2013).
23. Hölzer, A. & Sommerfeld, M. New simple correlation formula for the drag coefficient of non-spherical particles. *Powder Technol.* **184**, 361–365 (2008).
24. Belmonte, A., Eisenberg, H. & Moses, E. From flutter to tumble: inertial drag and Froude similarity in falling paper. *Phys. Rev. Lett.* **81**, 345–348 (1998).
25. Zhong, H. et al. Experimental investigation of freely falling thin disks. Part 1. The flow structures and Reynolds number effects on the zigzag motion. *J. Fluid Mech.* **716**, 228–250 (2013).
26. Kim, J. T., Jin, Y., Shen, S., Dash, A. & Chamorro, L. P. Free fall of homogeneous and heterogeneous cones. *Phys. Rev. Fluids* **5**, 093801 (2020).
27. Chigurupati, N. et al. Evaluation of red cabbage dye as a potential natural color for pharmaceutical use. *Int. J. Pharm.* **241**, 293–299 (2002).

28. Binnig, J., Meyer, J. & Kasper, G. Calibration of an optical particle counter to provide PM2.5 mass for well-defined particle materials. *J. Aerosol Sci.* **38**, 325–332 (2007).
29. Shao, W., Zhang, H. & Zhou, H. Fine particle sensor based on multi-angle light scattering and data fusion. *Sensors* **17**, 1033 (2017).
30. Heo, S. Y. et al. Wireless, battery-free, flexible, miniaturized dosimeters monitor exposure to solar radiation and to light for phototherapy. *Sci. Transl. Med.* **10**, eaau1643 (2018).
31. Kang, S. K., Koo, J., Lee, Y. K. & Rogers, J. A. Advanced materials and devices for bioresorbable electronics. *Acc. Chem. Res.* **51**, 988–998 (2018).
32. Lee, G., Choi, Y. S., Yoon, H. J. & Rogers, J. A. Advances in physicochemically stimuli-responsive materials for on-demand transient electronic systems. *Matter* **3**, 1031–1052 (2020).

Publisher's note Springer Nature remains neutral with regard to jurisdictional claims in published maps and institutional affiliations.

© The Author(s), under exclusive licence to Springer Nature Limited 2021

Methods

Three-dimensional (3D) micro-, meso- and macrofliers

Fabrication of 2D precursors in thin films of SMP (thickness $\sim 5 \mu\text{m}$) began with a mixture (a mass ratio of 7:3) of epoxy monomer (E44, molecular weight $\sim 450 \text{ g mol}^{-1}$, China Petrochemical Corporation) and curing agent (D230, poly(propylene glycol) bis(2-aminopropyl) ether, Sigma-Aldrich). Spin coating and thermal curing (100°C , 3 h) of this mixture onto a sacrificial layer of water-soluble polymer (spin cast; poly(4-styrenesulfonic acid, 500 nm), PSA; Sigma-Aldrich) on a silicon wafer defined a thin film of SMP. Electron beam evaporation of chromium and gold (Cr/Au, thickness $\sim 10/50 \text{ nm}$) followed by photolithography and wet etching formed a metal hard mask for patterned removal of exposed regions of the SMP by oxygen plasma reactive ion etching (O_2 RIE). Removing the Au and the underlying PSA facilitated the retrieval of the patterned SMP onto a water-soluble tape (polyvinyl alcohol, 3M Corporation). A multilayer of Ti/Mg/Ti/ SiO_2 (thickness $\sim 5/50/5/50 \text{ nm}$) deposited through a shadow mask by electron beam evaporation defined sites for chemical bonding, activated by exposure to ozone to create surface hydroxyl termination on the SiO_2 . Transfer onto a pre-strained silicone elastomer substrate (Ecoflex, Smooth-On) led to strong covalent bonding only at these locations, with weak van der Waals adhesion forces at all other regions. Releasing the prestrain led to mechanical buckling and a corresponding 2D to 3D geometric transformation. Heating to 70°C for 1 min in an oven followed by cooling to room temperature fixed the 3D shape via shape memory effects. Immersing the structure in water eliminated the Mg layer and released the structures as free-standing objects. The basic 3D fabrication approach applies equally well at large scales, up to systems with dimensions in the range of metres (ref. ¹⁸).

3D pH-responsive mesofliers

Fabrication of colorimetric pH-responsive 3D microfliers involved preparation of an anthocyanin aqueous solution of 0.2 wt% red cabbage extract (Fluxias GmbH) and infiltration ($\sim 1 \text{ mbar}$) through a polycarbonate (PC) membrane (0.2- μm pore size, 30- μm thickness, Fisher Scientific). Mechanical transformation of 2D precursors that consist of laser-patterned (LPKF4 UV laser system) bilayers of SMP/PC membrane bonded by hot pressing yielded the desired 3D structures.

3D electronic mesofliers

Fabrication of the silicon (Si) nanomembrane (NM) nMOS transistors began by defining regions of phosphorus doping using spin-on dopants (950°C , 8 min) on a silicon on insulator (SOI, top silicon thickness $\sim 200 \text{ nm}$, SOITEC) wafer for source and drain contacts. For Si NM diodes, the doping involved both phosphorus ($1,050^\circ\text{C}$, 15 min) and boron ($1,100^\circ\text{C}$, 30 min) to define p-n junctions. Removing the buried silicon dioxide (SiO_2) by wet etching released the top device silicon from the SOI wafer, and enabled transfer printing of the resulting Si NMs onto spin-cast films of polyimide (PI, thickness $\sim 3 \mu\text{m}$, HD microsystems Inc.) on a sacrificial layer of polymethylmethacrylate (PMMA, thickness $\sim 100 \text{ nm}$, MicroChem Inc.) on a silicon wafer. Photolithography and RIE (Plasma Therm, Inc.) with sulfur hexafluoride gas (SF_6 , 100 mtorr, 50 W, 40 standard $\text{cm}^3 \text{ min}^{-1}$, 200 s) left the top silicon only in the active regions of the device. A thin layer of SiO_2 (thickness $\sim 5 \text{ nm}$) formed by PECVD served as the gate dielectric for Si NM nMOS transistors. A bilayer of Cr/Au (thickness $\sim 5/100 \text{ nm}$) deposited by electron beam evaporation and patterned by photolithography served as electrodes and interconnects. Spin casting a thin layer of PI (thickness $\sim 3 \mu\text{m}$) and etching by RIE (O_2 gas, 150 mtorr, 100 W, 20 standard $\text{cm}^3 \text{ min}^{-1}$, 15 min) completed the formation of an ultra-thin active device layer composed of Si NM devices and metal interconnects. Dissolving the PMMA layer with acetone released the devices from the silicon wafer. Lastly, the Si NMs device layer encapsulated by a film of PI was transfer printed onto a thin film of SMP (thickness $\sim 5 \mu\text{m}$) using a PDMS stamp. Additional

steps to create 3D electronic mesofliers from these 2D precursors followed those outlined above. Layers of PI on the bottom and the top enhance the structural integrity of the SMP and improve the rigidity of the overall device. They also place the Si NM near the neutral mechanical plane to minimize the potential for fracture during assembly and use^{7,8}.

3D internet of things (IoT) macrofliers

Fabricating the 2D precursors began with spin-coating films of SMP (thickness $\sim 12 \mu\text{m}$) onto thick Cu foils (thickness $\sim 18 \mu\text{m}$). A pattern of photoresist served as a mask for wet etching (CE-100 etchant, Transene) the copper foil to define a metal interconnect structure for the electronic components. After using a laser cutting process to pattern the film of SMP, mounting an NFC chip (RF430FRL152HCRGER, Texas Instruments), a collection of photodiodes (PDB-CD160SM, Advanced Photonix), a set of MOSFETs (CSD17381F4, Texas Instruments), supercapacitors (CPH3225A, Seiko Instruments) and capacitors (GRM033R60J225ME47D/C0603X7R1A103K030BA and C0603X5R1A104K030BC, Murata Electronics North America/TKD) at defined locations on the 2D precursor with conductive epoxy (Allied Electronics) yielded a digital sensing system. Additional steps to create 3D IoT macrofliers from these 2D precursors followed those outlined above.

Optical experiments with particulate matter (PM) pollution

The 3D IoT macroflier uses a millimetre-scale, wireless, and battery-free NFC platform with an electronic circuit for accumulation mode dosimetry in the ultraviolet-A region of the solar spectrum, where the flux depends, in part, on airborne particulates. The photodiodes generate a photocurrent with a magnitude that correlates with the instantaneous exposure intensity. This current continuously charges the supercapacitor such that the accumulated charge, measured by the voltage, defines the exposure dose³⁰. A dust generation chamber operated with incense sticks, smoke cakes, corn starch and kitchen blenders served as a platform to investigate the influence of fine particulate pollution on the measured response (Extended Data Fig. 9).

Experiments using 3D-particle tracking velocimetry (3D-PTV)

The studies involved two types of measurements, both performed using 3D-PTV in a customized channel (Extended Data Fig. 6a): (1) 3D trajectories of free-falling microfliers with 2D, 3D and 3D porous designs; and (2) associated 3D induced flows. The upper part of the test chamber consisted of a 1.5-m-long glass tube with an inner diameter of 0.01 m to (i) minimize anomalous behaviours such as tumbling and (ii) ensure steady-state behaviour. The lower part included an acrylic glass enclosure with inner dimensions of $0.1 \text{ m} \times 0.1 \text{ m} \times 0.2 \text{ m}$ ($L \times W \times H$), sufficiently large to minimize boundary effects. The investigation volume for the fliers had dimensions of $4 \text{ cm} \times 4 \text{ cm} \times 6 \text{ cm}$, illuminated by an LED light source. The volume for visualizing 3D induced flows was $0.8 \text{ cm} \times 0.8 \text{ cm} \times 1.2 \text{ cm}$, illuminated by a synchronized dual-cavity Nd:YLF laser with pulse energies of 50 mJ at repetition rates of 1 kHz (S27-80-M, Terra). Oil droplets with diameters of the order of $1 \mu\text{m}$ served as tracers. Recordings for 3D-PTV experiments used three digital cameras ($2,560 \times 1,600$ pixels CMOS Phantom Miro 340 with 12 GB on-board memory and frame rates of 1,000 f.p.s.). A series of lenses (60 mm, focal ratio $f/2.8$, Nikon AF Micro-Nikkor) focused the images on the corresponding investigation volumes. Pre-processing, calibration, 3D reconstruction, tracking and post-processing exploited 3D-PTV codes have been described previously³³. Tracking of the 3D reconstructed positions of fliers relied on the Hungarian algorithm linked by performing a three-frame gap closing to produce long trajectories. Associated temporal derivatives were filtered and estimated using fourth-order B splines. Additional details of the PTV system can be found elsewhere³⁴. The free-falling experiments involved 10 repetitions for each sample to obtain statistically significant measurements of the stability and kinematics of the falling behaviours (Fig. 3c). Tracer particles were tracked in 3D and converted into inferred 3D Eulerian velocity vector fields that

defined the 3D induced flows. Interpolating scattered Lagrangian flow particles at each frame based on the natural neighbour interpolation method yielded the 3D vector fields.

The 3D wake structures measured with 3D-PTV highlight additional features. Two representative instants in time (Fig. 3d and Supplementary Fig. 17) show flow separations and momentum deficits, as highlighted by the blue (flow structures in the opposite direction of the fall) and red (flow structures in the direction of the fall) isosurfaces, respectively. The wake for the 2D flier exhibits comparatively large and small flow structures against and along the motion, respectively, at this instant and at other times throughout the fall. The 3D mesoflier induces comparatively small and rotating flow structures oriented against the motion, with large following structures. Large flow structures against the fall in the 2D precursor indicate early flow separation, which promotes comparatively high pressure gradients and aerodynamic instabilities. Small structures in the direction of the fall indicate small momentum deficits and, consequently, low drag and correspondingly large v_r . The rotational dynamics of the 3D mesofliers minimize flow separation and induce large momentum deficits, resulting in stable and slow falling behaviours (Supplementary Video 6).

Experiments using high-speed particle image velocimetry (PIV) and a vertical wind tunnel

Two sets of experiments used high-speed PIV above a vertical wind tunnel (Extended Data Fig. 6b) to define the wake dynamics of (1) fixed 2D precursors and 3D fliers exposed to flow velocities of $U \approx 0.4 \text{ m s}^{-1}$, similar to those associated with terminal velocities in free fall, and (2) working 3D fliers with five different diameters $d = 1, 2, 3, 4$ and 5 cm at $U \approx 1.2, 2.4$ and 3.6 m s^{-1} . A 200 μm diameter and 4 cm long wire with adhesive on the tip fixed the positions of the fliers (Supplementary Fig. 16). The wire was attached to a thin rectangular acrylic plate to minimize boundary effects on incoming flows. A customized vertical wind tunnel enabled measurements of wake dynamics around the fliers. A series of four fans (G8015X12B-AGR-EM, Mechatronics) placed on the bottom of the tunnel produced air flows in the wind tunnel. A tunable power supply (TP3005N Regulated DC Variable Power Supply, Tekpower), calibrated by quantifying the background flow using PIV, set the fan speed. The channel consisted of flow straighteners above the fans to smooth the flows and an aluminium honeycomb grid above the contraction section. A 1/8-inch acrylic sheet machined by laser cutting defined the frame of the tunnel. A high-speed PIV system (TSI, Inc.) characterized the wake induced by meso- and macrofliers. Olive oil droplets served as tracers in the air. A 1 mm thick laser sheet produced by a synchronized dual-cavity Nd:YLF laser with pulse energies of 50 mJ at repetition rates of 100 Hz (S27-80-M, Terra) illuminated the resulting flows. The field of view covered a 24.48 mm \times 15.3 mm region above the fliers, with 950 image pairs collected for each case at a frequency of 100 Hz using a digital camera (2,560 \times 1,600 pixels, CMOS Phantom Miro 340). A recursive cross-correlation method (Insight 4G software, TSI Image) processed pairs of images. The first pass used a 64 pixel \times 64 pixel interrogation window. The final window had a size of 8 pixels \times 8 pixels with 50% overlap, resulting in a vector spacing $\Delta x = \Delta y = 0.0765 \text{ mm}$. For 15 sets of PIV measurements on working fliers (three speed and five diameters), the field of view covered a 128 mm \times 80 mm region with a vector spacing of $\Delta x = \Delta y = 0.4 \text{ mm}$. Overall, more than 97% of the vectors were resolved in all measurements.

The aerodynamics of these 3D IoT macrofliers (Fig. 4g–i and Supplementary Figs. 27–30) are consistent with preceding discussions of the physics. The wakes exhibit oscillating tip vortices in the vicinity of the wings and a secondary vortex behind the centre (Fig. 4g and Supplementary Video 7). Mean streamwise velocity fields (Fig. 4h) are similar to those of mesofliers with similar designs. Figure 4i shows that across a range of centimetre-scale dimensions, the normalized

transverse velocity profiles exhibit self-similarity, allowing for efficient dimensional analysis and modelling.

Finite element analysis

Three-dimensional FEA techniques quantitatively captured the mechanical deformations and the associated 3D configurations of the fliers in different scales, during processes of compressive buckling and bending under the flow of air. Eight-node shell elements were employed using commercial software (ABAQUS), with refined meshes to ensure computational accuracy. Linear elastic responses were used to model the SMP, with material parameters Young's modulus $E_{\text{SMP}} = 2 \text{ MPa}$ and Poisson's ratio $\nu_{\text{SMP}} = 0.3$. Parameters for the other materials were $E_{\text{Cu}} = 110 \text{ GPa}$, $\nu_{\text{Cu}} = 0.3$ and yield strength $\sigma_y = 350 \text{ MPa}$ as a perfect elastic-plastic model for copper, $E_{\text{Si}} = 190 \text{ GPa}$ and $\nu_{\text{Si}} = 0.29$ as an elastic model for silicon.

Computational fluid dynamics

Three-dimensional CFD simulations defined the rotational falling behaviours of the fliers in a static state, using the 3D rotating machinery, laminar flow module in commercial software (COMSOL 5.2). First-order discretization (P1-P1) with a refined mesh ensured computational accuracy. Fliers with 3D configurations defined by FEA resided in the centred rotating region inside a large tube. The inflow velocities set at the bottom surface of the outer tube matched values equivalent to the terminal velocities of the fliers. The flier was set as the 'rotating interior wall' in the rotating domain, as shown in Supplementary Fig. 3, where the local velocity of air equals the velocity of flier. The rotating speed of the rotating domain, which represents the rotating velocity of the flier, corresponded to the value for which the torque of the air acting on the microflier equals zero. For a given terminal velocity, the force of air acting on the flier in the inflow direction matched its weight. The air was modelled as compressible flow, with properties at sea level air density $\rho = 1.225 \text{ kg m}^{-3}$ and dynamic viscosity $\mu = 17.89 \text{ } \mu\text{Pa s}$. At large Reynolds numbers, the k- ω model captured the effects of turbulence. Two-dimensional CFD simulations captured the aerodynamic behaviours of the 2D aerofoils in a similar manner (Supplementary Fig. 18). CFD simulations show that multiple fliers can be released simultaneously with non-interacting aerodynamics provided that the separation distances are more than 10 flier diameters, where the wake is fully recovered (Fig. 4i, Supplementary Fig. 2).

Electromagnetic simulations

Commercial software ANSYS HFSS was used to perform electromagnetic finite element analysis and to determine the inductance Q factor for the 2D and 3D antennas, magnetic field distribution and power transfer from a nearby antenna. Lumped ports yielded the port impedance Z of the antennas. An adaptive mesh (tetrahedron elements) and a spherical radiation boundary (radius of 1,000 mm) ensured computational accuracy. The inductance (L) and Q factor (Q) (shown in Supplementary Fig. 24) were obtained from $L = \text{Im}\{Z\}/(2\pi f)$ and $Q = |\text{Im}\{Z\}|/\text{Re}\{Z\}$, where $\text{Re}\{Z\}$, $\text{Im}\{Z\}$ and f represent the real and imaginary part of the Z and the operating frequency, respectively. The approximate power P_{out} in the flier coil is calculated from the S-parameters (shown in Extended Data Fig. 10) by varying the vertical distance between the coil and a high-frequency (HF) transmission antenna as

$$\eta_{21} = \frac{P_{\text{out}}}{P_{\text{in}}} = \frac{|S_{21}|^2(1 - |\Gamma_L|^2)}{\left[1 - |(1 - |\Gamma_L|^2)|^2\right](1 - S_{22}\Gamma_L^2)} \times 100$$

where P_{in} is the power of the transmission antenna, $\Gamma_L = \frac{Z_L - Z_0}{Z_L + Z_0}$ is the reflection coefficient from the load, Z_L is the impedance of the load, and $Z_0 = 50 \text{ } \Omega$ is the reference impedance. The default material properties included in the HFSS material library were used in the simulation.

Data availability

The data that support the findings of this study are available from the corresponding author on reasonable request.

33. Kim, J. T., Nam, J., Shen, S., Lee, C. & Chamorro, L. P. On the dynamics of air bubbles in Rayleigh-Bénard convection. *J. Fluid Mech.* **891**, A7 (2020).
34. Kim, J. T. & Chamorro, L. P. Lagrangian description of the unsteady flow induced by a single pulse of a jellyfish. *Phys. Rev. Fluids* **4**, 064605 (2019).

Acknowledgements This work was supported by the Querrey Simpson Institute for Bioelectronics at Northwestern University. B.H.K. acknowledges support from the following: National Research Foundation of Korea (NRF) grants funded by the Korean government (MSIT) (nos 2019R1G1A1I100737, 2020R1C1C1014980); the Nanomaterial Technology Development Program (NRF-2016M3A7B4905613) through the National Research Foundation of Korea (NRF) funded by the Ministry of Science, ICT and Future Planning; the Project for Collabo R&D between Industry, Academy and Research Institute funded by Korean Ministry of SMEs and Startups in 2020/2021 (project no. S2890749/S3104531); the Nano-Material Technology Development Program through the National Research Foundation of Korea (NRF) funded by the Ministry of Science, ICT and Future Planning (2009-0082580); the National Research Facilities and Equipment Center at the Ministry of Science and ICT (Support Program for Equipment Transfer, grant no. 1711116699); and the Glint Materials Company. K.L. acknowledges support from the State Key Laboratory of Digital Manufacturing Equipment and Technology, Huazhong University of Science and Technology (grant no. DMETKF2021010). Y.P. acknowledges support from the German Research Foundation (PA 3154/1-1). Y.Z. acknowledges support from the National Natural Science Foundation of China (grant no. 12050004), the Institute for Guo Qiang, Tsinghua University (grant no. 2019GQG1012), and the Tsinghua National Laboratory for Information Science and Technology. H.L. acknowledges support from the Creative Materials Discovery Program through the National Research Foundation of Korea (NRF) funded by the Ministry of Science and ICT (NRF-2018M3D1A1058972). S.M.W. acknowledges support from the National Research

Foundation of Korea funded by the Ministry of Science and ICT of Korea (NRF-2021M3H4A1A01079367), and by the Nano Material Technology Development Program (2020M3H4A1A03084600) funded by the Ministry of Science and ICT of Korea. Y.H.J. acknowledges support from the research fund of Hanyang University (HY-202100000000832). C.H.L. acknowledges funding support from the National Science Foundation (2032529-CBET). Z.X. acknowledges support from the National Natural Science Foundation of China (grant no. 12072057), the LiaoNing Revitalization Talents Program (grant no. XLYC2007196), and Fundamental Research Funds for the Central Universities (grant no. DUT20RC(3)032). R.A. acknowledges support from the National Science Foundation Graduate Research Fellowship (NSF grant number 1842165) and a Ford Foundation Predoctoral Fellowship. We thank Jaeeun Koo for artwork in Fig. 1a.

Author contributions B.H.K., K.L., J.-T.K. and Y.P. contributed equally to this work. Y.H., L.P.C., Y.Z. and J.A.R. conceived the ideas and supervised the project. B.H.K., K.L., J.-T.K., Y.P., Y.H., L.P.C., Y.Z. and J.A.R. wrote the manuscript. H.J., X.W., S.M.W., H.-J.Y., G.L., W.J.J., K.H.L., Y.H.J., S.Y.H., Y.L., J.K., Y.K., Y.Y. and X.Y. performed microelectromechanical experiments. J.-T.K., T.C. and P.P. performed fluid dynamics experiments. Z.X., T.S.C., R.A., H.L., H.S., F.Z., Y.Z. and L.C. performed mechanical and electromagnetic modelling and simulation. S.H.H., J.K., S.J.O., H.L. and C.H.L. provided scientific and experimental advice. All authors commented on the manuscript.

Competing interests The authors declare no competing interests.

Additional information

Supplementary information The online version contains supplementary material available at <https://doi.org/10.1038/s41586-021-03847-y>.

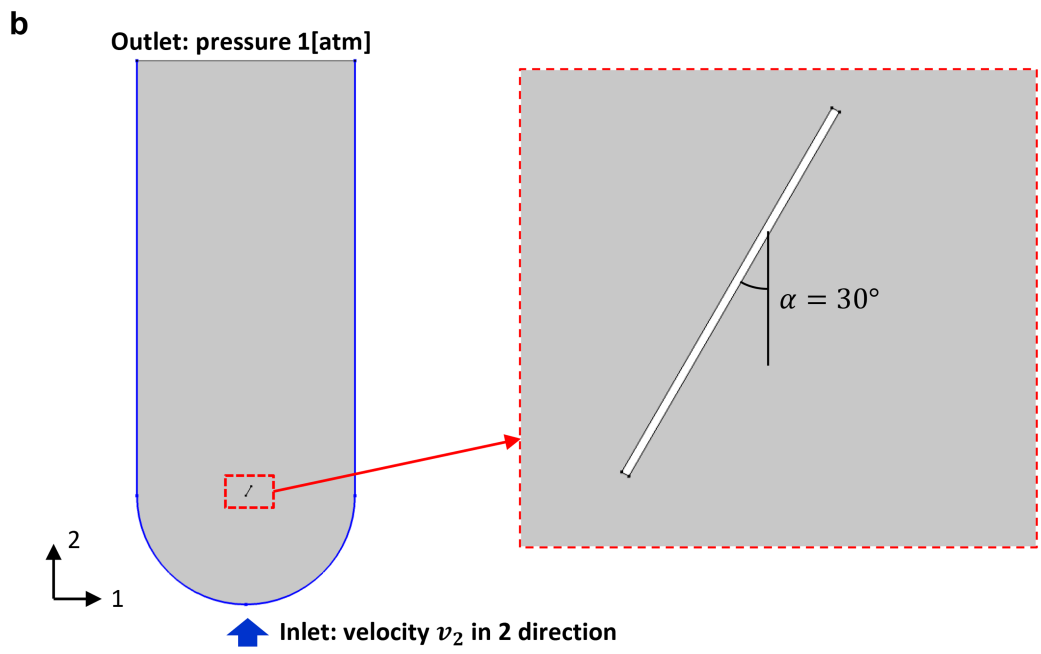
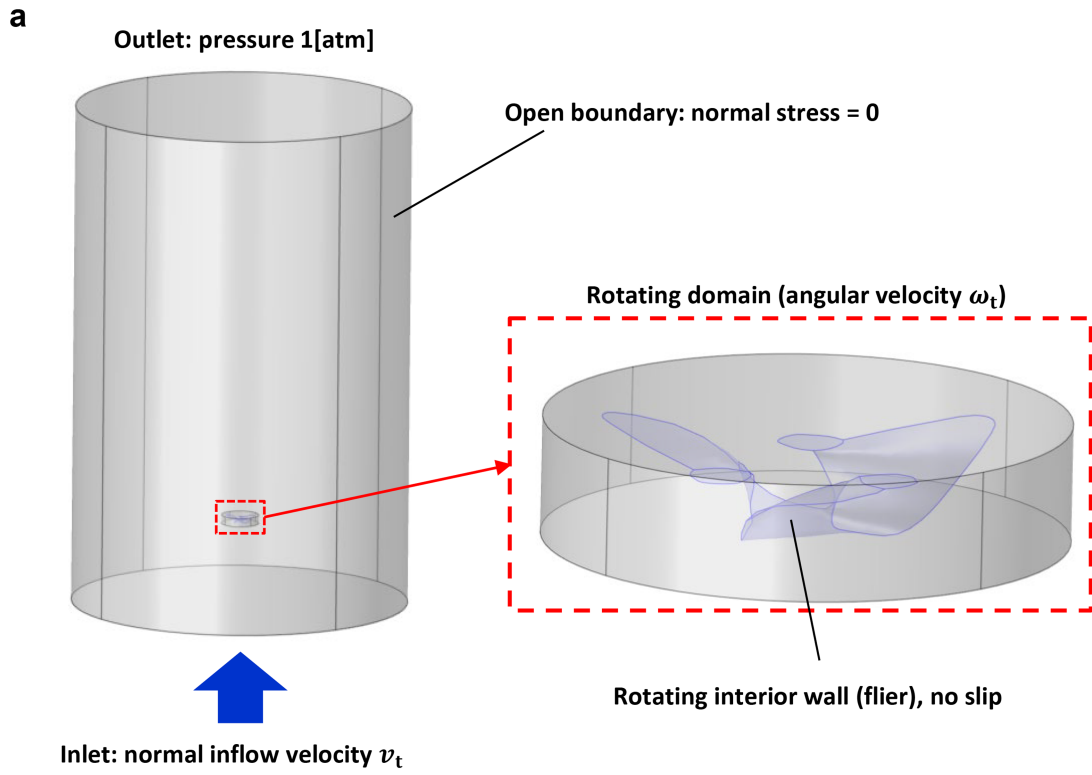
Correspondence and requests for materials should be addressed to Yonggang Huang, Leonardo P. Chamorro, Yihui Zhang or John A. Rogers.

Peer review information Nature thanks Elizabeth Helbling and the other, anonymous, reviewer(s) for their contribution to the peer review of this work. Peer reviewer reports are available.

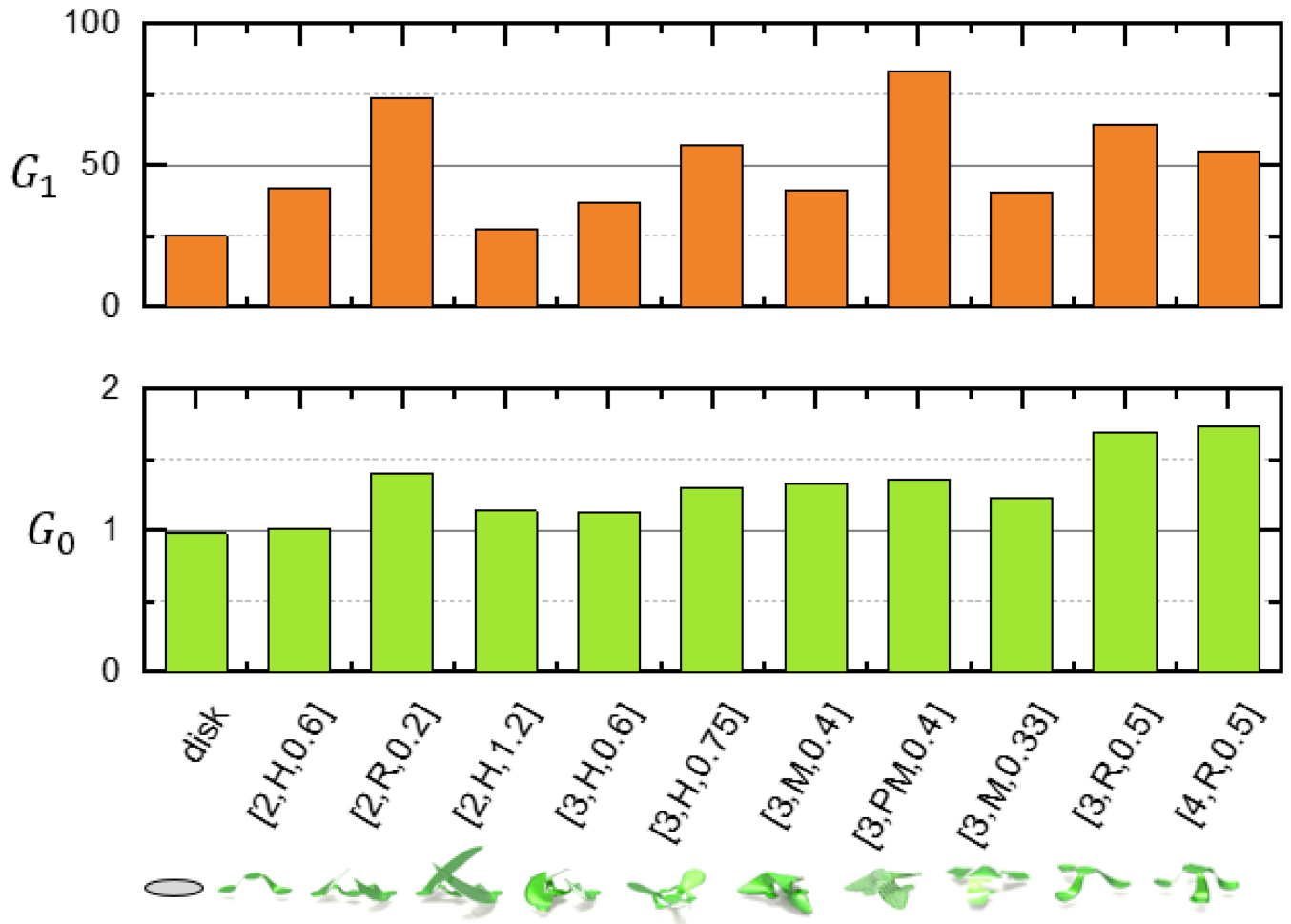
Reprints and permissions information is available at <http://www.nature.com/reprints>.



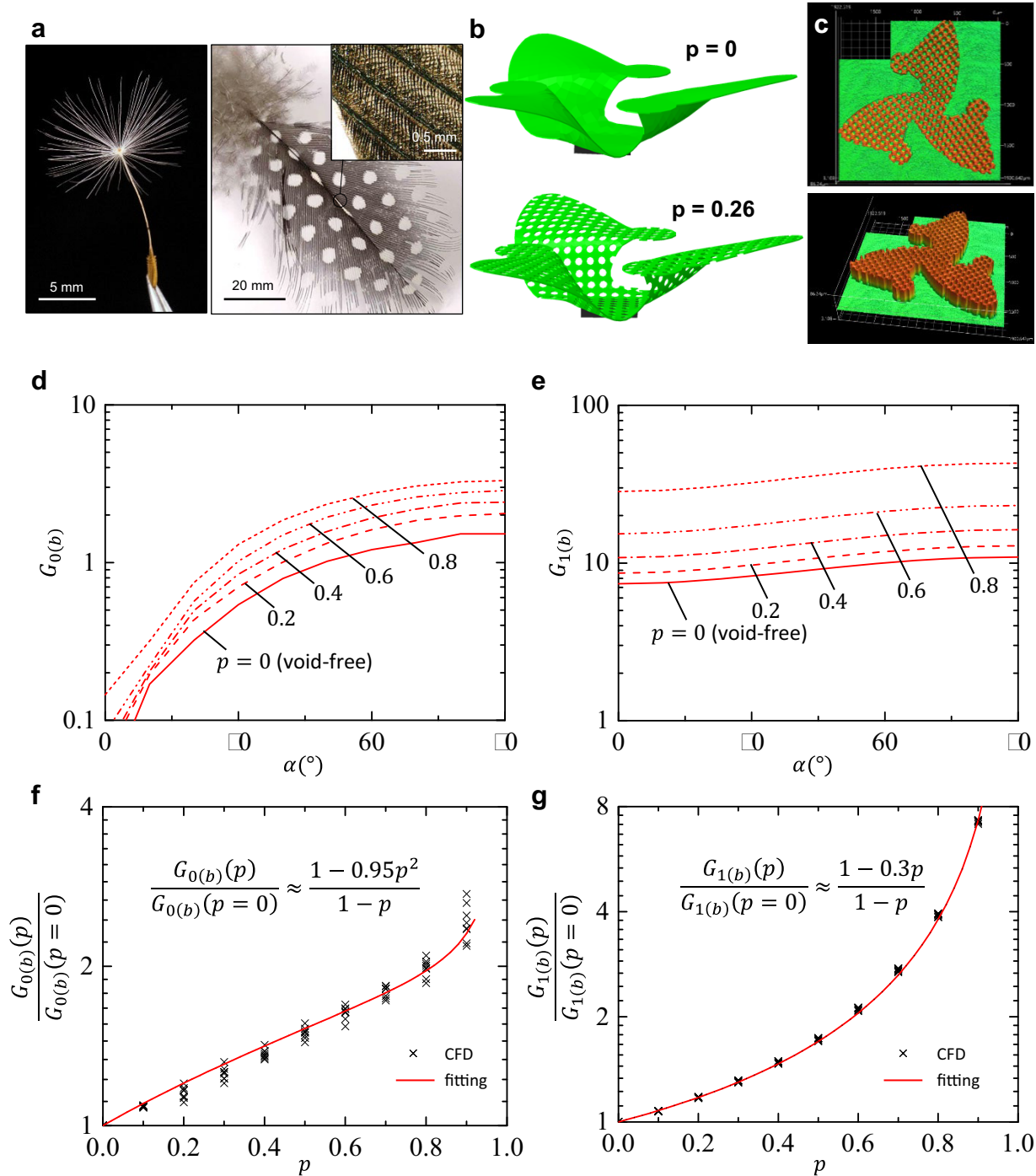
Extended Data Fig. 1 | Bio-inspired 3D micro- and mesofliers. Photographs of a 10 × 10 array of 3D micro- and mesofliers.



Extended Data Fig. 2 | Schematic diagram of the configuration for computational fluid dynamics simulation. (a) 3D rotational falling fliers and (b) 2D aerofoil.

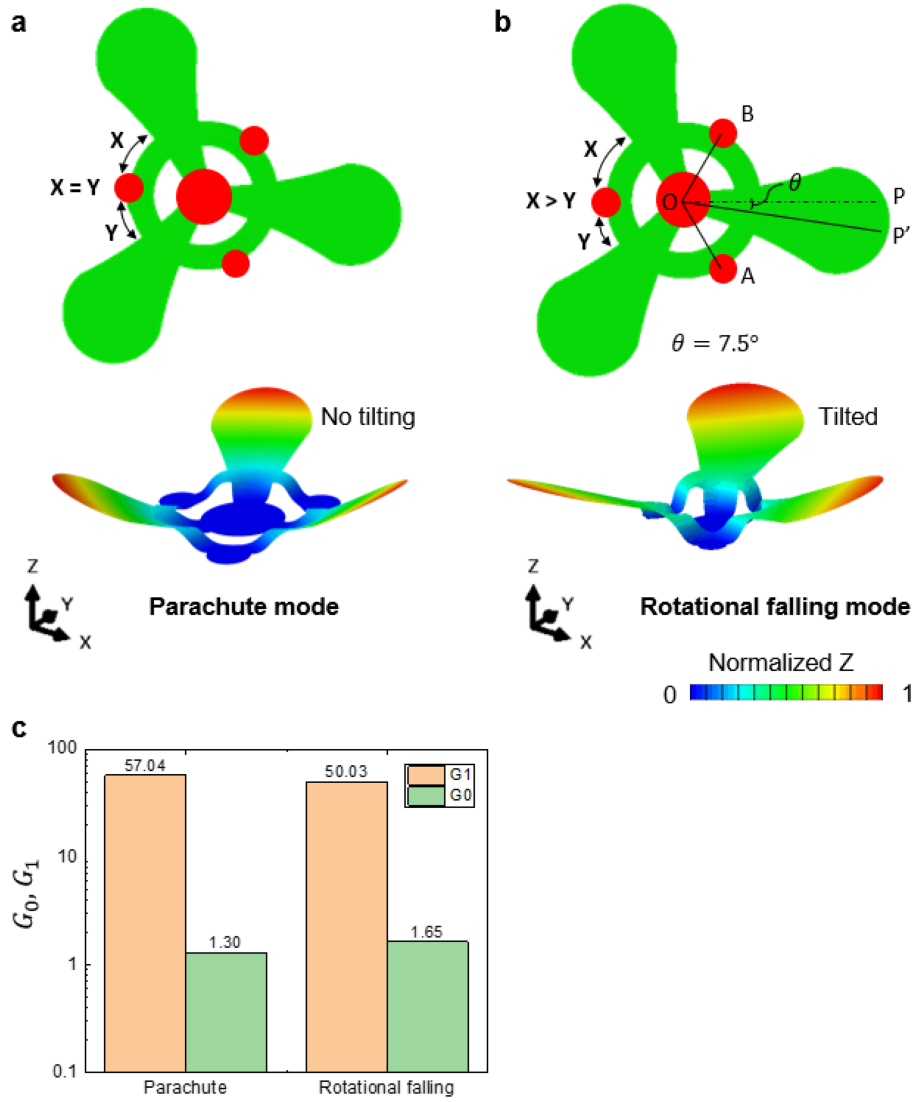


Extended Data Fig. 3 | Comparison of G_0 and G_1 across all classes of fliers. CFD simulation results for the components G_0 and G_1 of the drag coefficient C_D , for fliers of types R, H, M and PM, with the 2D disk as a comparison.

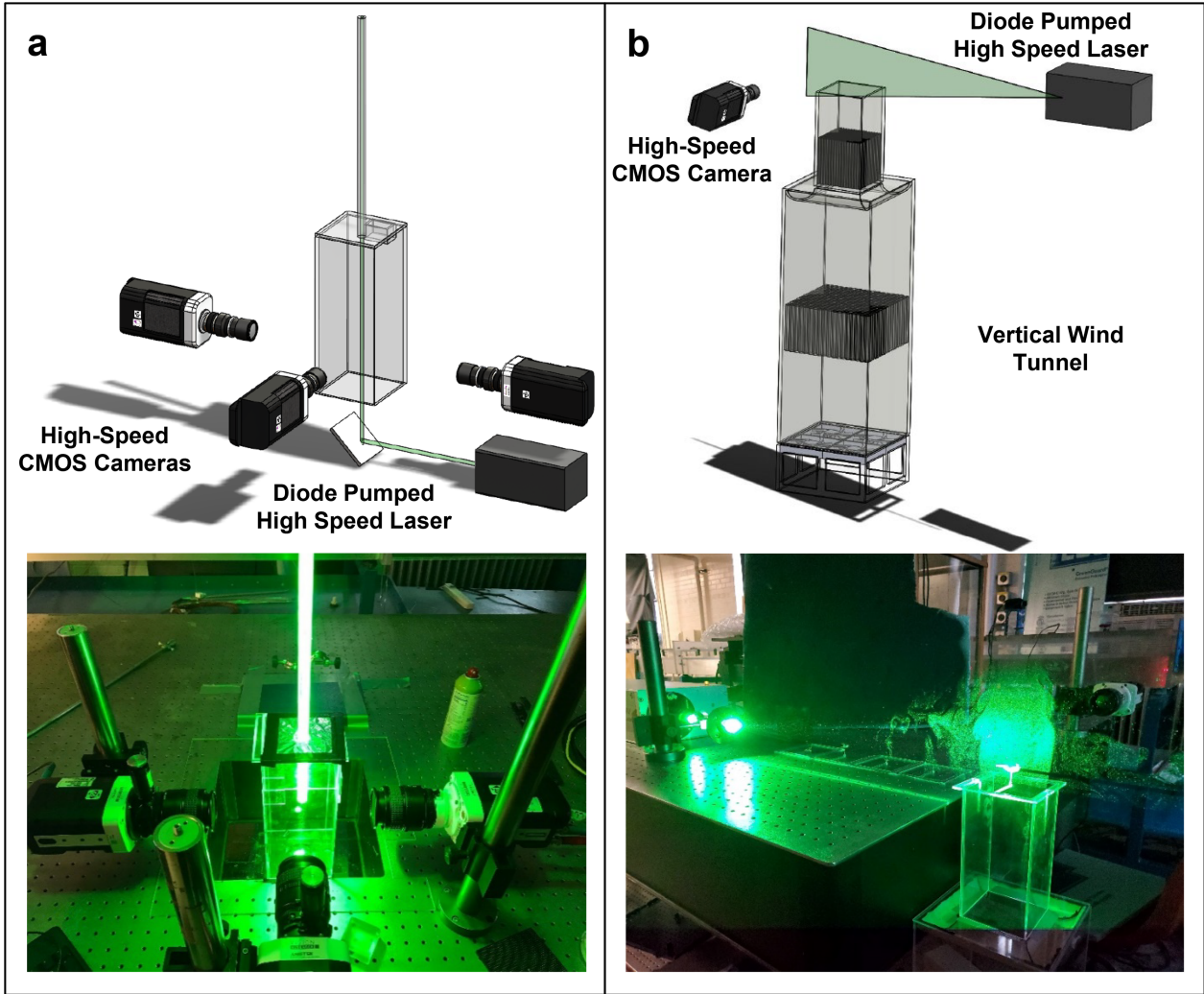


Extended Data Fig. 4 | 3D microflier with porous design. (a) Inspiration of porosity from nature: optical images of dandelion seeds and a feather. (b) FE simulated configuration of a 3D void-free microflier ($p = 0$) and a 3D microflier of porosity design ($p = 0.26$). (c) Images of scanned thickness of a 2D precursor

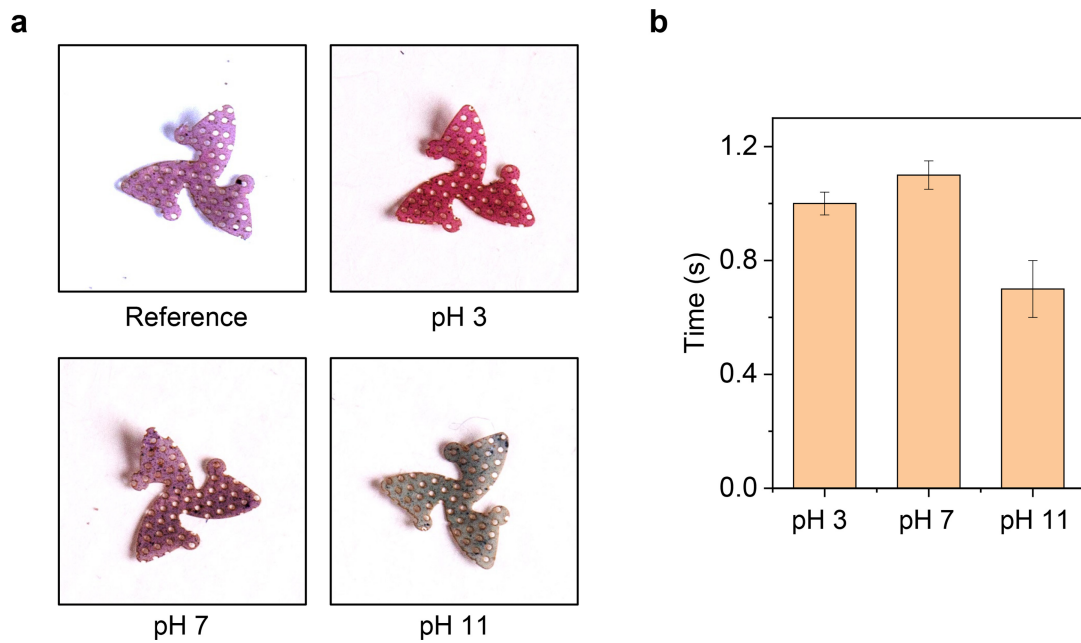
for a porous microflier, with top view and perspective view, respectively. (d) $G_{0(b)}$ and (e) $G_{1(b)}$ versus the attack angle for various porosities. Normalized (f) $G_{0(b)}$ and (g) $G_{1(b)}$ over their void-free values versus porosity, with the CFD values of various $\alpha \in [0^\circ, 90^\circ]$ and analytic fittings.



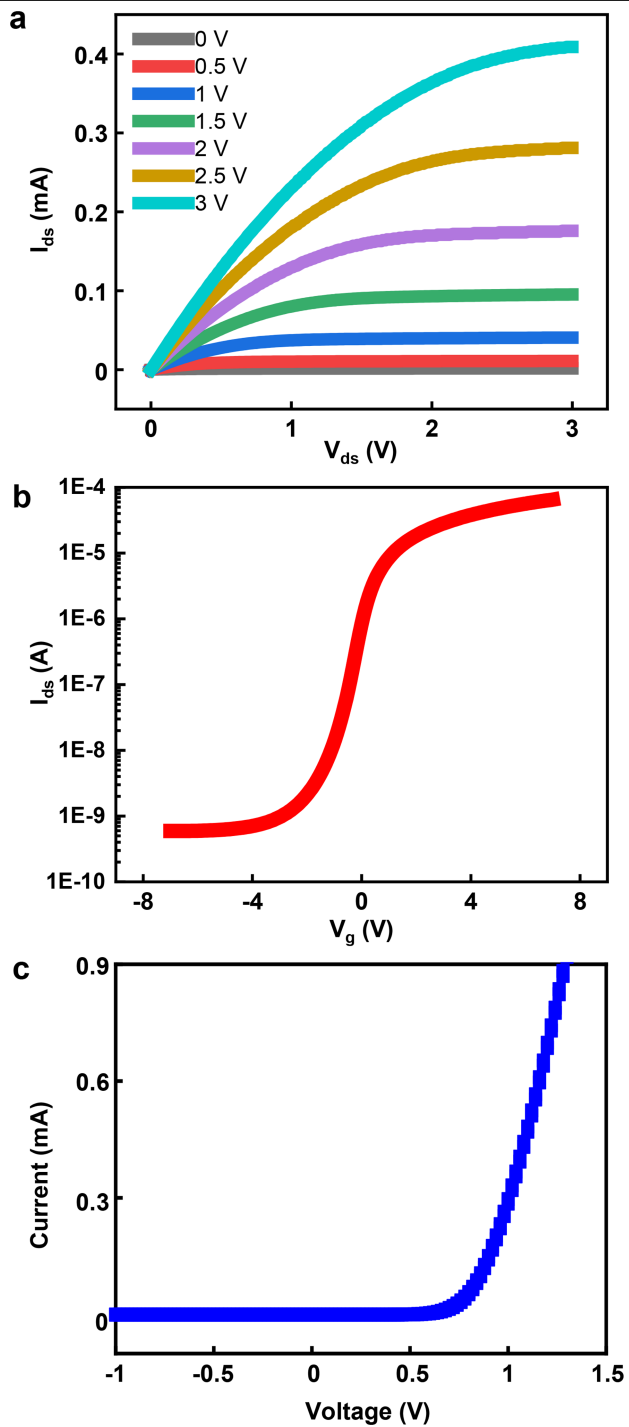
Extended Data Fig. 5 | Mechanical simulation of a 3D microflier [3, H, 0.75]. Schematic images of (a) a parachute design where the blades have no rotational tilting, and (b) a rotating flier design with rotationally tilted blades. (c) Comparison of G_0 and G_1 between the parachute mode and rotational falling mode.



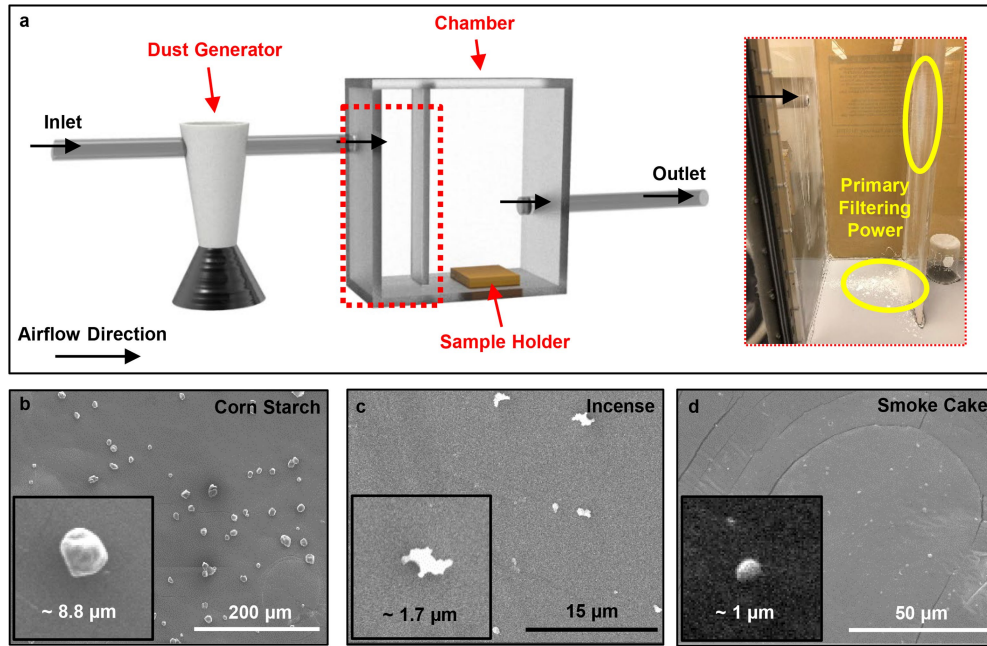
Extended Data Fig. 6 | Experimental setups. (a) Schematic (top) and photograph (bottom) of 3D-PTV experiment on free-falling mesofliers and (b) schematic (top) and photograph (bottom) of high speed PIV experiment on fixed 3D IoT fliers above a wind tunnel.



Extended Data Fig. 7 | Changes in colour of a pH-responsive 3D mesoflier. (a) Photographs of pH-responsive 3D mesoflier immersed in different buffer solutions with pH ranging from 3 to 11. (b) Response time of pH indicators after immersion into buffer solutions at different pH values.

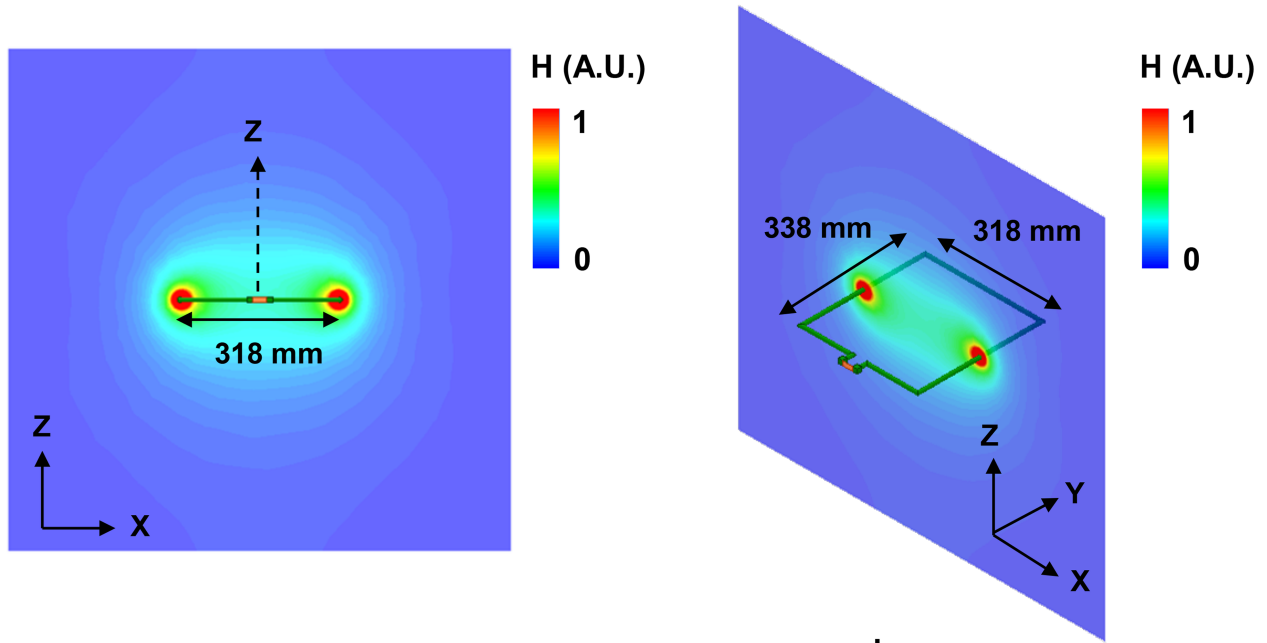


Extended Data Fig. 8 | The electrical characteristics of SiNM n-channel transistor (channel width/length = 80/20 μm) and diode integrated with 3D mesoflinders. (a) Drain current as a function of source/drain voltage for the gate voltages from 0 to 3 V. (b) The log scale transfer curves as a function of gate voltage from -7 to 7 V. (c) Current-voltage characteristics of a diode.

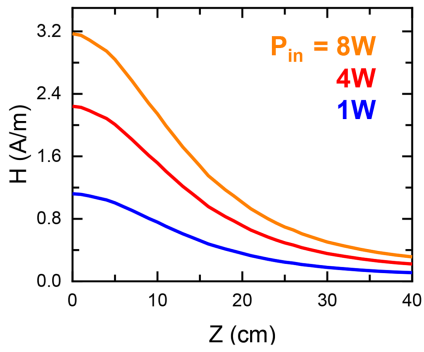


Extended Data Fig. 9 | Experiments for particulate matter (PM). (a) A dust generation chamber operated with kitchen blenders. Scanning electron microscope (SEM) images of fine dust generated by (b) corn starches, (c) incenses and (d) smoke cakes.

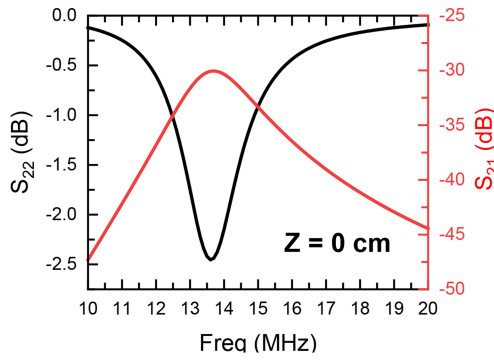
a



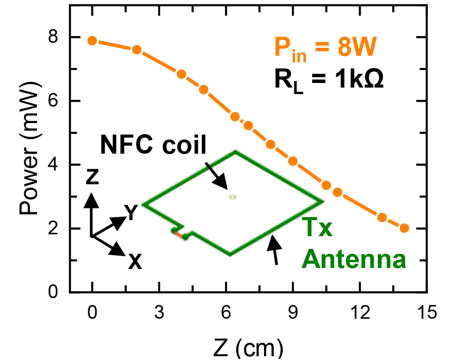
b



c



d



Extended Data Fig. 10 | Electromagnetic performance of coils for wireless power transmission. (a) Normalized magnetic field generated by the commercial transmission antenna with dimensions (318 mm × 338 mm × 30 mm). (b) Magnetic field strength along the line (0,0,Z) as a function of the distance Z normal to the transmission antenna for different input power P_{in} (1, 4, and 8 W).

(c) Scattering parameters for the electromagnetic energy transfer between the coils when the NFC coil is located at the centre of the transmission antenna (0,0,0). (d) Simulated power in the NFC coil at different distance Z normal to the primary antenna with $P_{in} = 8$ W.